Mei-yu front assessment in CMIP6 earth system models during the East Asian summer monsoon

International Journal of Climatology

International Journal of Climatology | RMetS

RESEARCH ARTICLE OPEN ACCESS

Mei-yu Front Assessment in CMIP6 Earth System Models During the East Asian Summer Monsoon

Kelvin S. Ng[1] | Gregor C. Leckebusch[1] | Kevin I. Hodges[2] | Yaocun Zhang[3]

[1]School of Geography, Earth and Environmental Sciences, University of Birmingham, Birmingham, UK | [2]Department of Meteorology, National Centre for Atmospheric Science, University of Reading, Reading, UK | [3]School of Atmospheric Sciences, Nanjing University, Nanjing, China

Correspondence: Kelvin S. Ng (k.s.ng@bham.ac.uk)

Received: 4 June 2024 | **Revised:** 17 February 2025 | **Accepted:** 18 February 2025

Funding: This study was supported by the UK-China Research and Innovation Partnership Fund through the Met Office Climate Science for Service Partnership (CSSP) China as part of the Newton Fund.

Keywords: CMIP6 | East Asian Summer Monsoon | Mei-yu front

ABSTRACT

The East Asian Summer Monsoon (EASM) plays a pivotal role in redistributing water across East Asia, including contributing a considerable flood risk due to the potential for localized extreme precipitation. To gain insights into future EASM changes, it is crucial to explore the dynamics of a core driver of extreme precipitation during the EASM, the Mei-yu front (MYF). While prior studies have examined various aspects of EASM in climate models, the comprehensive assessment of the dynamically important, that is, MYF remains largely unexplored. In this study, we evaluate the Mei-yu front representation in 38 CMIP6 models from May to August using the ECMWF Reanalysis version 5 (ERA5) as reference. Our findings reveal that several CMIP6 models struggle to accurately reproduce the MYF climatology, with performance varying by month. By categorizing models based on the east–west bias of MYF position in May, we identify distinct monthly evolutions in these biases during the EASM season. Our study shows a significant association between the misrepresentation of the MYF climatology in CMIP6 models and the misrepresentation of the Western North Pacific High, particularly its western edge. Other potential sources of biases are based on the misrepresentation of other large-scale circulation patterns, such as the South Asian High, and are also investigated. Furthermore, the performance evaluation of different aspects of the EASM is compared to previous studies, and the transferability of those principle evaluation findings is discussed.

1 | Introduction

Understanding any potential changes in precipitation over East Asia is important as it has a significant impact on the socio-economic development and human life of over 1.6 billion people (United Nations 2022). One of the major drivers of extreme precipitation in this region is the so-called Mei-yu front (MYF), which is a core dynamical feature of the East Asian Summer Monsoon's (EASM) regional establishment. It is responsible for over 45% of total summer rainfall in the lower-middle Yangtze River valley (Ding and Chan 2005). In particular, a record-breaking amount of extreme Mei-yu precipitation, which caused more than 100 billion RMB direct economic loss (Wei et al. 2020), was observed in 2020 (Ding et al. 2021). A good understanding of the physical mechanisms that could lead to the occurrence of similar events would be crucial in the context of hazard evaluation, especially to increase the hazard preparedness for potential future climate conditions.

Many studies have investigated the potential changes in various aspects of the EASM, such as the occurrence probability of the related extreme precipitation events (Zhou et al. 2021; Wu et al. 2023), and the large-scale circulation patterns in East Asia (Wainwright et al. 2021; Yang et al. 2022; Horinouchi

et al. 2023) in the future climate using climate model simulations from the Coupled Model Intercomparison Project phase 5/6 (CMIP5/6). Many of the above studies utilized multi-model ensembles (MME) of CMIP5/6 models to generate a mean estimate. These approaches aim to exploit the available model simulations to capture uncertainties in the potential changes across different scenarios and models, and thus provide a mean projection of the EASM in an anthropogenic future climate. However, besides the issue of model dependency (Kuma et al. 2023), the projections based on MME strongly depend on the capability of the individual models to correctly simulate various features of the EASM as well as the respective dynamical features and large-scale circulation. Consequently, to understand the usefulness of MME-based statements, it is necessary to understand the individual model's ability to simulate these specific aspects of the EASM.

Nevertheless, studies focussing on the evaluation of an individual model's capability of simulating specific aspects of the EASM do reveal many models might have significant biases, including the variability of regional to large-scale circulation. Park et al. (2020) investigated the long-term change in the EASM lifecycle of 32 CMIP6 model historical simulations using precipitation. They have shown that in general CMIP6 models underestimate the intensity of monsoon precipitation and have limited ability to simulate the climatological EASM precipitation evolution and its variability, but there are a few models that can simulate the rainband propagation and the long-term intensification of EASM precipitation relatively well. Piao et al. (2023) analysed the climatological northern boundary of the EASM, which is defined as the 2 mm/day isoline of the extended summer (May to September) precipitation, in the historical simulation of 45 CMIP6 models and they found that the northern boundary of the EASM for most models is too far north in comparison to observations. This, in turn, produces a northward bias in the summer precipitation pattern. The cause of these biases is linked to the westward extension of the Western North Pacific Subtropical High (WNPSH) and the northward shift of the subtropical westerly jet (Piao et al. 2023). Bu et al. (2022) evaluated the boreal summer circulation patterns in the Asian region, using 500 hPa geopotential height, of 140 variants of CMIP6 model simulations from 23 different models using a self-organising map approach. They identified a large spread in skill to re-produce the large-scale circulation pattern in Asia. They further pointed out that using model outputs with low skill could lead to errors in extreme event evaluation. While these studies focused on various aspects of the EASM, to the authors' knowledge, none of them evaluated one of the major dynamical mechanisms in triggering extreme precipitation over East Asia, that is, the MYF. An evaluation of MYF climatology in climate models is important: While the climatological spatial distribution of precipitation during the EASM season in climate models could be similar to reanalysis, they exhibit noticeable discrepancies in their representation of the core dynamical mechanism—the MYF. These discrepancies appear in MYF intensity, as well as its longitudinal and zonal positioning across models (Figure S1). This would indicate that the EASM-related precipitation in climate models would be correct for the wrong reasons. This would in fact produce potentially misleading statements about the potential future climate change of extreme precipitation.

Furthermore, Ng et al. (2022, 2024) developed a causality-guided statistical approach to skilfully derive extreme MYF precipitation based only on indices of known large-scale climate modes. They speculated that the performance of the causality-guided statistical approach could be improved if more observations were available. They further suggested that the application of the so-called Unprecedented Simulation of Extremes with Ensembles (UNSEEN) approach (Osinski et al. 2016; Thompson et al. 2017; Ng and Leckebusch 2021) could be used to increase the number of observations by using physically consistent event sets generated by climate models. This suggestion could only apply if the MYF climatology in climate models is similar to observations. However, to the authors' knowledge, this has not been systematically investigated yet.

An investigation of the representation of the MYF in climate models is thus necessary as it would address one of the major issues in generating reliable actionable information from climate models—even though the historical simulation of certain climate models can generate similar climatological EASM precipitation patterns as in reanalysis and observations, are these models generating the correct precipitation pattern because of the correct reasons? If these models are not generating the pattern for the correct reasons, then incorrect information from these models could be used in hazard evaluation. Consequently, it would hinder the hazard preparedness for potential future climate conditions.

This study aims to fill this gap with the following objectives: (1) evaluation of how well the representation of the MYF climatology is in 38 CMIP6 models in the core EASM period of May to August; (2) investigation of the potential links between biases in the representation of the MYF climatology in climate models and biases in the presentation of certain circulation patterns, such as the North Pacific High (NPH); (3) exploration of the transferability of the performance evaluation of (mis)representation of different facets of climate models that are closely associated with the EASM.

The study is organized as follows: The description of data and methods can be found in Section 2. Results of the evaluation of the representation of CMIP6 MYF climatology and analyses of the potential sources of biases in CMIP6 simulations are presented in Section 3. A brief discussion, including the origin of the biases and transferability of performance evaluation, can be found in Section 4, while Section 5 presents our summary and concluding remarks. The full names of acronyms used in this study can be found in Appendix A.

2 | Data and Method

The European Centre for Medium-Range Weather Forecasts (ECMWF) fifth generation reanalysis (ERA5) data (Hersbach et al. 2020), for the period 1979–2014, is used as the reference climatology. Historical (1979–2014) simulations of 38 CMIP6 (Eyring et al. 2016) models (Table 1) are evaluated. Instead of using output from only one member from each of the available models, we make use of all available model members, which are accessible to us, to construct an ensemble climatology for each model. This approach reduces the possibility of analysing an outlier member and consequently better captures the potential systematic bias of themodels.

TABLE 1 | List of CMIP6 model outputs used in this study.

Model	Number of members	Reference
ACCESS-CM2	1	Bi et al. (2020)
ACCESS-ESM1-5	1	Ziehn et al. (2020)
AWI-ESM-1-1-LR	1	Sidorenko et al. (2015), Rackow et al. (2018)
BCC-ESM1	1	Wu et al. (2020)
CanESM5	1	Swart et al. (2019)
CESM2	9	Danabasoglu et al. (2020)
CESM2-WACCM	3	
CMCC-CM2-HR4	1	Cherchi et al. (2019)
CMCC-CM2-SR5	1	
CMCC-ESM2	1	
CNRM-CM6-1	10	Voldoire et al. (2019)
CNRM-ESM2-1	5	Séférian et al. (2019)
EC-Earth3	1	Döscher et al. (2022), Massonnet et al. (2020)
EC-Earth3-AerChem	1	
EC-Earth3-CC	1	
EC-Earth3-Veg-LR	1	
FGOALS-f3-L	1	He et al. (2020)
FGOALS-g3	1	Li et al. (2020)
GFDL-CM4	1	Held et al. (2019)
HadGEM3-GC31-LL	5	Williams et al. (2018), Andrews et al. (2020)
HadGEM3-GC31-MM	4	
IITM-ESM	1	Swapna et al. (2018)
INM-CM4-8	1	Volodin et al. (2018)
INM-CM5-0	1	Volodin et al. (2017)
IPSL-CM6A-LR	9	Boucher et al. (2020)
IPSL-CM6A-LR-INCA	1	
KACE-1-0-G	1	Lee et al. (2020a)
MIROC6	1	Tatebe et al. (2019)
MPI-ESM-1-2-HAM	1	Tegen et al. (2019), Neubauer et al. (2019)
MPI-ESM1-2-HR	1	Gutjahr et al. (2019)
MPI-ESM1-2-LR	1	
MRI-ESM2-0	1	Yukimoto et al. (2019)
NESM3	1	Cao et al. (2018)
NorESM2-LM	1	Seland et al. (2020)
NorESM2-MM	1	
SAM0-UNICON	1	Park et al. (2019)
TaiESM1	1	Lee et al. (2020b)
UKESM1-0-LL	16	Sellar et al. (2019)

Note: Simulation outputs with incomplete coverage of years were not used.

The MYF was detected by a scheme developed by Befort et al. (2016, 2017). This scheme is an extension of the Baiu front detection scheme developed by Tomita et al. (2011). The MYF identification scheme locates the daily position of the MYF by detecting the minimum of the product of the meridional gradient of the daily equivalent potential temperature and the specific humidity at the 850 hPa level. The detailed description of the MYF detection scheme is available in Ng et al. (2022). Since the detection scheme returns a latitude–longitude position of the MYF at a given time, to enable easier and better comparison of the MYF position climatology between ERA5 and CMIP6 historical simulations, a monthly climatological MYF detection density is calculated. Analogous to the so-called cyclone track density (Befort et al. 2020; Ng and Leckebusch 2021), the MYF detection density is defined as the number of times the MYF is detected within a 2.5° radius of a given grid box per month. Based on this definition, the MYF detection density can also be interpreted as the probability of observing the MYF in a specific grid box in a particular month. For example, for the same grid box, if the model MYF detection density is 0.5 and the ERA5 MYF detection density is 0.8, it indicates the MYF is 30% more likely to be found at this grid box in ERA5 in comparison to the model. Consequently, this allows us to evaluate the representation of the climatological spatial distribution of the MYF position in CMIP6 models on a monthly basis.

For a quantitative assessment of the deviation of the CMIP6-derived monthly MYF detection density climatology in a basin-wide perspective, the monthly MYF detection density climatological mean centre of action (hereinafter CoA) is introduced. This is defined as the weighted mean position, that is, latitude and longitude, of the monthly climatological MYF detection density weighted by the value of the MYF detection density itself. We define the MYF detection density climatology of a model as having a significant bias in latitude (longitude) if the CoA latitude (longitude) anomaly is larger than 1° N (1° E) or smaller than 1° W (1° S).

3 | Results

3.1 | Evaluation of the Monthly Mei-yu Front Detection Density Climatology

The monthly MYF detection density shows significant model-to-model variability during the season (cf. Figure 1 example for June; Figure S2 for all other months; both figures show

anomalies relative to ERA5). To provide a clearer view of the time-varying nature of the model bias, in Figure 2 we show the CoA latitude anomalies and CoA longitude anomalies for CMIP6 models in different months as a scatter plot.

For the May MYF detection density climatology (Figure S2a), 17 models show significant northward bias (Figure 2a), in particular for East China. This indicates that the onset of the MYF season in these 17 models, that is, extreme precipitation over the Yangtze River basin, occurs much earlier than in observations in these models, which usually occurs in late June. Furthermore, 17 models show significant eastward bias in the position of MYF detection density climatology (Figure 2a). For the June MYF detection density climatology (Figure S2b), the significant northward bias persists in 12 models and eight models show significant southward bias (Figure 2b). Meanwhile, the significant eastward bias in the position of MYF detection density climatology remains for 16 models, with four models having a CoA longitude anomaly larger than 4° E. For the July and August MYF detection density climatology (Figure S2c,d), the number of models with significant northward bias reduces to seven and six, respectively (Figure 2c,d). The number of models with significant southward bias increases to 11 for the July MYF detection density climatology (Figure 2c), whereas only six models have significant southward bias for the August MYF detection density climatology (Figure 2d).

Furthermore, 38 CMIP6 models can be divided into two groups—Westward Bias (WB; blue letters in Figure 2) and Eastward Bias (EB; red letters in Figure 2), based on whether their CoA longitude anomalies in May are less than 0° E (Group WB) or greater than 0° E (Group EB). Although the definition of the groups might seem arbitrary, the time evolution of the CoA position biases has very different behaviour. First, a comparison of the bias of CoA longitude position in May and June shows that models in group WB tend to reduce their westward bias, whereas models in group EB tend to increase their eastward bias (Figure 2a,b). Second, for the July and August MYF detection density climatology, the eastward bias of 18 models in group EB worsens, with five and seven models having CoA longitude anomalies larger than 6° E, respectively (Figure 2c,d). The IPSL-CM6A-LR-INCA model has the largest eastward bias with ca. 8° E and ca. 10° E for the July and August MYF detection density climatology, respectively. This is partially due to the fact that some models generate much fewer and/or shorter occurrences of the MYF in comparison to ERA5 (Figure S2c). While some models show significant southward bias, few models demonstrate biases over central north China (Figure S2c,d). In comparison to the previous months, models in group EB have a much larger increase in eastward bias than models in group WB. There are two factors that contribute to the positional bias of the MYF: (i) the zonal extent of the MYF; and (ii) the occurrence rate of MYF formation. These factors are linked to physical processes, which are discussed in Section 3.2.

The time evolution of the mean MYF detection density position bias of group WB and group EB demonstrates very different behaviour (Figure 3). While models in both groups tend to have increasing CoA longitude biases in the subsequent months, the magnitude of increase from May to August for group EB is 3.11° E, which is ca. 3.06 times larger than the magnitude of increase from May to August for group WB, which is 1.02° E (Figure 3). In addition, models in group WB have a CoA longitude bias less than 1.1° E independent of the month of interest, whereas models in group EB have significantly larger CoA longitude biases (Figures 1 and 2). The group behaviour also suggests that the biases of MYF detection density are directly related to certain systematic deficiencies in the models, which could be identifiable as early as May. Consequently, a potential source of bias is investigated in Section 3.2.

To quantitatively summarize the relative bias of the MYF position in CMIP6 models, rankings (Table 2) were done based on root mean squared differences (RMSD) between MYF detection density climatology of CMIP6 historical simulations and ERA5 for each month within the East Asia domain (90°–150° E; 15°–60° N) (Figure S2) as well as an overall ranking using the mean RMSD of all months. Consequently, based on the overall ranking, EC-Earth3-CC, EC-Earth3-Veg-LR, EC-Earth3-AerChem, CMCC-CM2-SR5 and TaiESM1 belong to the top five models.

Besides the north–south bias in the MYF detection density, many models have an east–west bias of the westward extent in MYF detection density climatology and from the impact perspective, a significant amount of precipitation associated with the MYF occurs over China, where the east–west bias occurs. Similar rankings could be created using a domain focusing on East China (90°–125° E), yet the resultant rankings for the respective months are very similar to the rankings shown in Table 2 with a Kendall tau correlation coefficient (τ) ranging from 0.84–0.94 for the respective months as well as the overall ranking. Furthermore, with the exception of a few outliers, models in group WB have higher rankings than models in group EB (Table 2). Around 85% of the models in group WB can be found in the top half of the ranking table, whereas only 11% of the models in group EB can be found in the top half of the ranking table. Since the grouping criteria are based purely on the CoA longitude anomaly, this confirms that the main deviations in the MYF detection density climatology often occur over the East China domain, which is where the eastward bias of the MYF detection density occurs. Those models in group WB that do not fit into this observation, such as AWI-ESM-1-1-LR, MPI-ESM-1-2-HAM, INM-CM4-8 and IITM-ESM, either have noticeable westward biases (CoA longitude anomaly < -1.96° E) in July and August and/or large northward biases (CoA latitude anomaly > 2.1° N) in May and June. On the other hand, CNRM-ESM2-1 and CNRM-CM6-1 are the models in group EB that can be found in the top half of the ranking table. While their overall CoA anomalies might be displaced to the east, they have relatively good ability in producing MYF with similar frequency and position over the eastern edge of the front (Figure S2xxv,xxvi).

It should be noted that models in the same model family (c.f. Figure 2; Kuma et al. 2023) tend to have similar rankings with the exception of the models in the CESM family. For example, models in the HadGEM family, such as ACCESS-CM2, ACCESS-ESM1-5, HadGEM3-GC31-LL, HadGEM3-GC31-MM, KACE-1-0-G and UKESM1-0-LL, are ranked at 37, 35, 32, 30, 36 and 33, respectively. This might suggest there is a systematic bias in the representation of the East Asia atmospheric circulation in the HadGEM system. A discussion regarding the systematic bias can be found in Section 4.

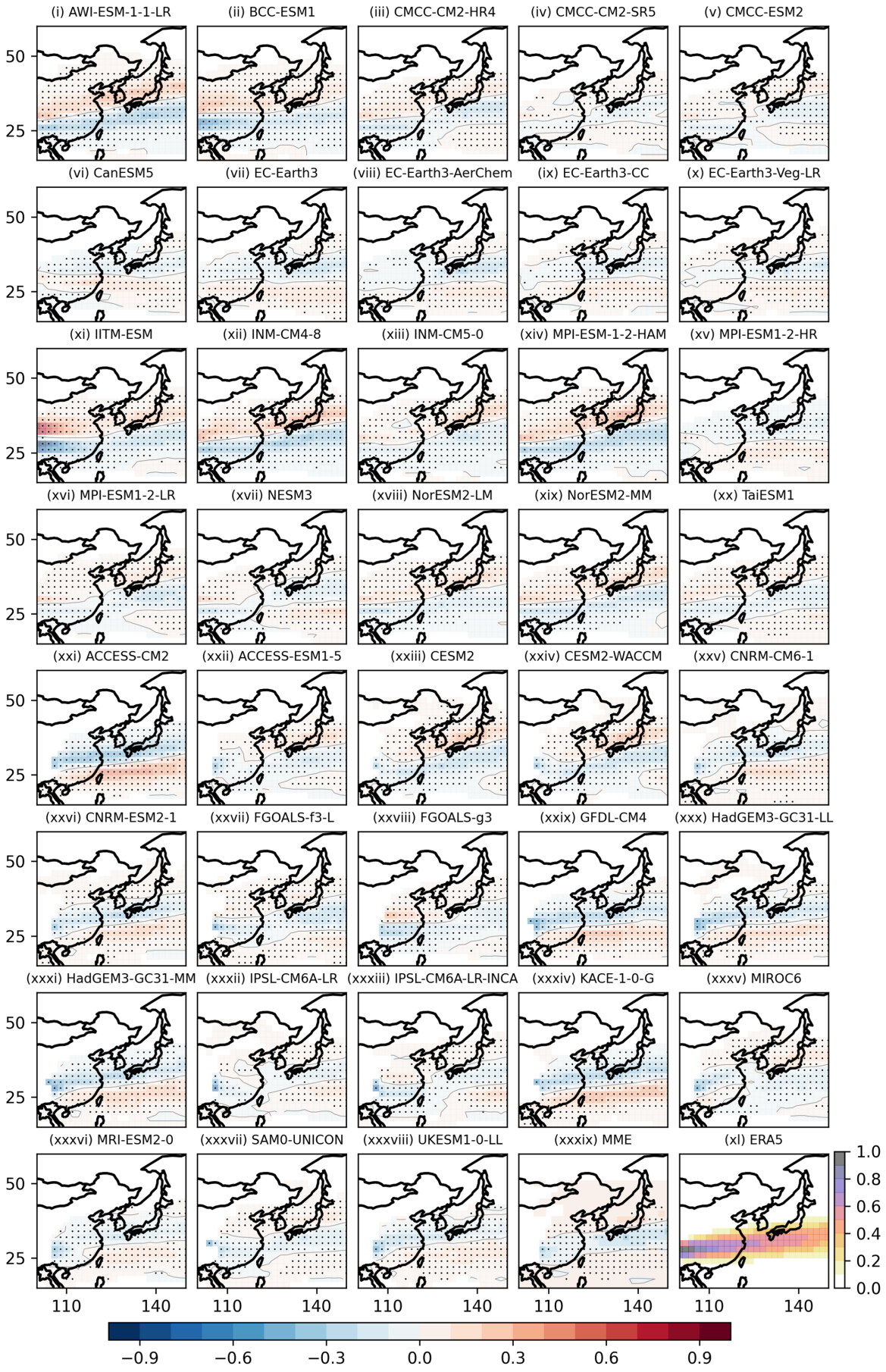

FIGURE 1 | Legend on next page.

FIGURE 1 | (i–xxxix) Monthly Mei-yu front (MYF) detection density climatology anomaly between CMIP6 historical simulations and ERA5 for June. Positive (warm colour) and negative (cold colour) indicate more and less likely to observe MYF in a model simulation than ERA5, respectively. The grey lines indicate the zero contours. Panels (i–xx) show models in group westward bias in alphabetical order. Panels (xxi–xxxviii) show models in group eastward bias in alphabetical order (see Table 2 for group labelling). Panel (xxxix) shows the multi-model ensemble mean. Panel (xl) shows the ERA5 monthly MYF detection density climatology of the respective month. Black dots indicate the difference of MYF detection density between model and ERA5 are significant at 0.05 level based on *t*-test. [Colour figure can be viewed at wileyonlinelibrary.com]

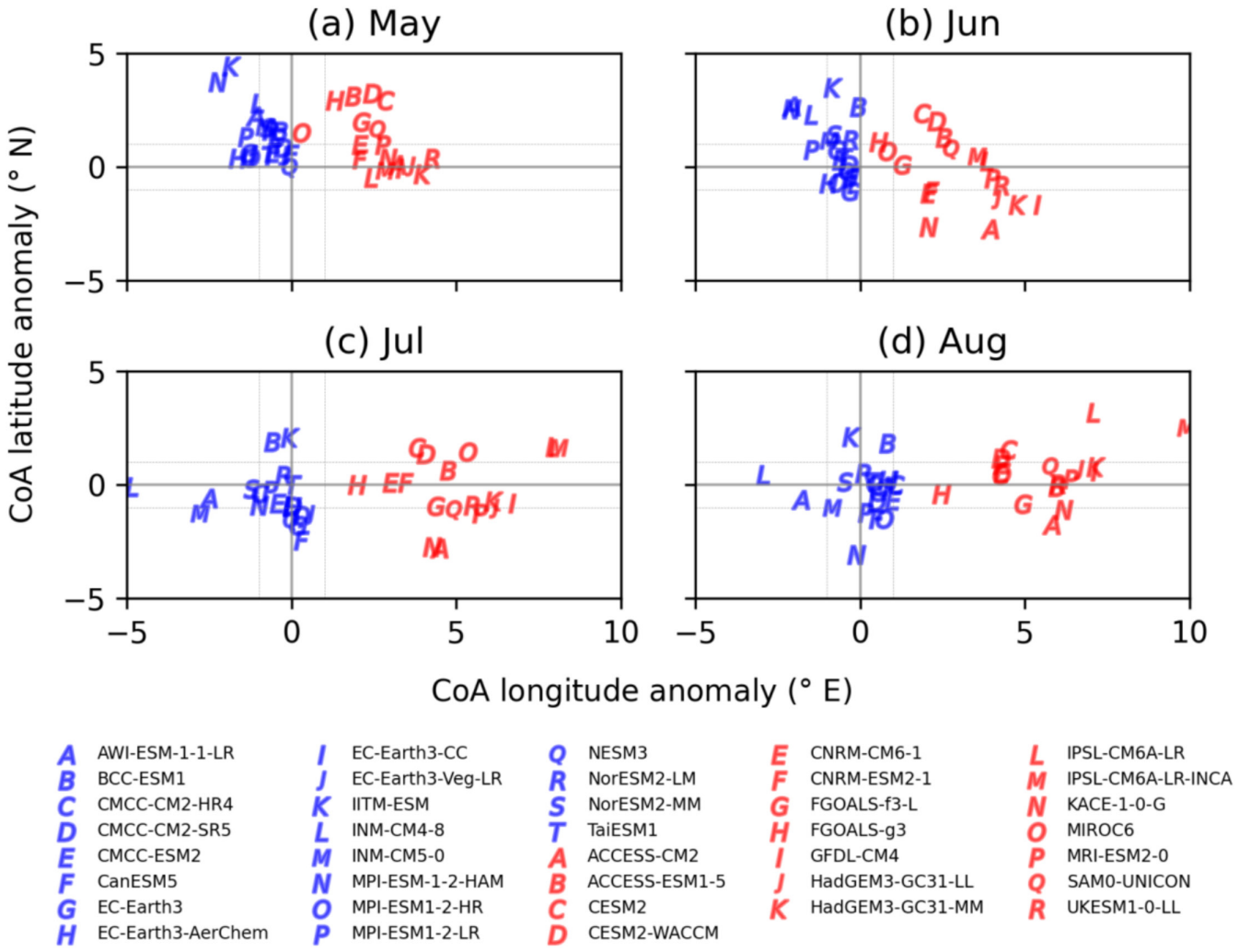

FIGURE 2 | Scatter plot of the centre of action anomaly of CMIP6 models with respect to ERA5 for (a) May, (b) June, (c) July and (d) August. Blue and red indicate models in group westward bias and eastward bias, respectively (see Section 3.1 for description). The solid grey horizontal and vertical lines indicate 0 latitude anomaly and 0 longitude anomaly, respectively. The dotted grey horizontal and vertical lines indicate ±1° latitude and longitude anomaly, respectively. [Colour figure can be viewed at wileyonlinelibrary.com]

3.2 | Potential Sources of Climatological MYF Detection Density Biases in CMIP6 Simulations

To investigate the source of the bias in the CMIP6 MYF detection density climatology, the representation of the North Pacific High (NPH) in the respective models has been examined. This is because the western edge of the NPH, that is, WNPSH, is known to have a significant influence on the formation and position of the MYF (Ding et al. 2020). Furthermore, it plays a major role in controlling the large-scale atmospheric flow configuration over East Asia.

Throughout the EASM season, the western edge of the NPH retreats eastward, and the centre of action of the western edge shifts northward (Figure S3). This leads to increases in the northward extent of moisture transport (Figure S4), and the position of moisture convergence is thus shifted to the northern part of East Asia; consequently, there is a northward propagation of the MYF during the EASM season. Since the MYF forms in a specific large-scale atmospheric configuration, the deviation of the representation of the NPH in CMIP6 models from ERA5 (Figure S5) will result in deviations of the MYF detection density climatology in CMIP6 models relative

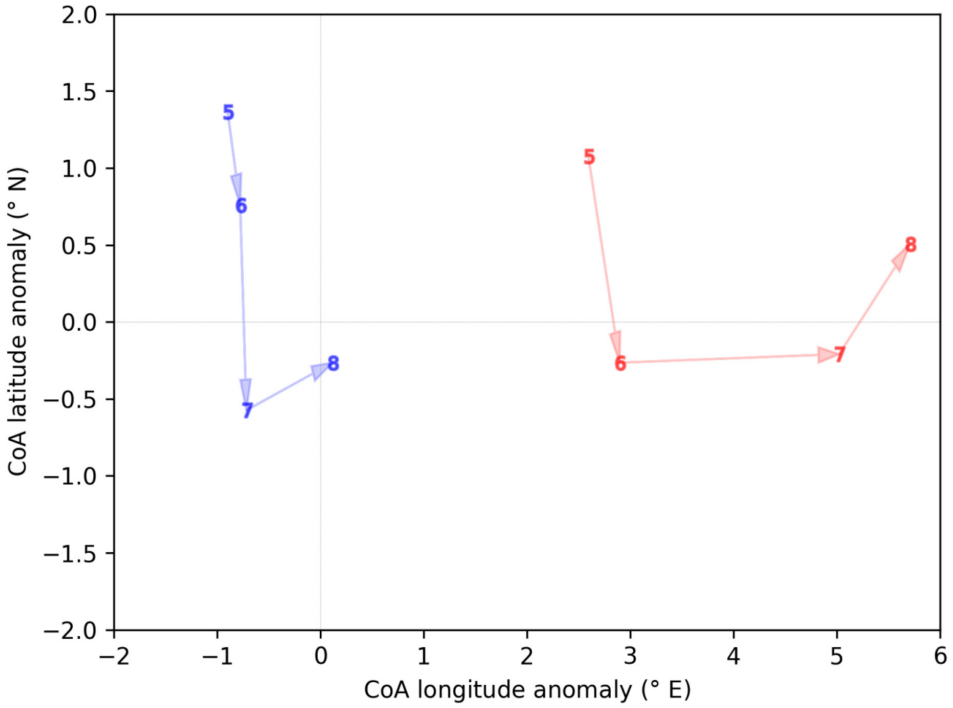

FIGURE 3 | The evolution trajectory of the mean group position bias of group westward bias (blue) and group eastward bias (red). The numbers indicate group mean CoA position anomalies of the month. [Colour figure can be viewed at wileyonlinelibrary.com]

to ERA5 (Figure S2) due to changes in moisture transport (Figure S6).

3.2.1 | Representations of North Pacific High for Groups Westward Bias and Eastward Bias

In order to highlight the contrast in the circulation differences between models in groups WB and EB, monthly climatological composite anomalies are constructed using models with significant CoA east–west positional bias (Figures 4 and 5). While there is intra-model variability in the climatological geopotential height anomalies (Figure S5), these composites provide a clearer picture regarding the potential source of biases of the MYF detection density in models for the respective groups and thus increase the interpretability of the results. Furthermore, almost all the models in group EB have significant CoA eastward bias for all months of interest (Table S1), whereas models in group WB have either significant CoA westward bias or no significant east–west bias in CoA, with the exception of EC-Earth3-Veg-LR and CMCC-CM2-HR4 where significant eastward bias in CoA is identified in August (Table S1).

Figure 4 shows composites of 850 hPa geopotential height anomalies of group EB (Figure 4a,d,g,j) and group WB (Figure 4b,e,h,k), with respect to ERA5 monthly climatology. In the EB composites (Figure 4a,d,g,j), except for the May composite, there exist spatially extensive negative anomalies over the west of the central north Pacific; whereas in the WB composites (Figure 4b,e,h,k), there exists a basin-wide dipole pattern with positive anomalies in the north and/or northwest side of the north Pacific, and negative anomalies in the south and/or southwest side of the north Pacific. Comparing the 850 hPa geopotential height composites of EB and WB (Figure 4c,f,i,l) shows a dipole pattern where negative/positive anomalies are observed in the northern/southern side of the north Pacific, showing a systematic difference between the NPH representation for the models with eastward CoA bias and westward CoA bias.

To quantitatively assess and diagnostically analyse the relationship between the deviation of the NPH representation and deviation of the MYF detection density climatology in the CMIP6 models relative to ERA5, the cross-model Pearson's correlation coefficient (r) between CoA and the WNPSH indices (Lu 2002), WNPSH-W and WNPSH-N are used. The WNPSH-W and WNPSH-N are defined as the 850 hPa geopotential height anomalies, with respect to ERA5, averaged over 10°–30° N, 110°–150° E (black box in Figure S3a), and 30°–40° N, 120°–150° E (green box in Figure S3a), respectively. These indices, WNPSH-W and WNPSH-N, are recognized for their ability to capture the westward and northward extension of the western edge of the NPH, respectively.

The east–west bias of the MYF detection density in the CMIP6 models during June to August shows a significant correlation with the WNPSH-N indices, as indicated in Table 3, where the correlation coefficient (r) ranges from −0.456 (p-value = 0.0040) to −0.535 (p-value = 0.0005). At first glance, this may appear counterintuitive, as one might expect that the westward extension of the WNPSH would be more related to the east–west bias of the MYF detection density. However, this relationship is in fact reasonable. The calculation domain of WNPSH-N covers the region of Japan, the southern part of the Sea of Japan, and the Yellow Sea. This region aligns with the largest differences in the composite of geopotential height anomalies between EB

TABLE 2 | Table of rankings of the goodness of CMIP6 models in simulating Mei-yu front (MYF) climatology based on root mean squared differences (RMSD) between monthly MYF detection density climatology of CMIP6 model historical outputs (1979–2014) and ERA5 (1979–2014) for the East Asia domain (90°–150° E) of different months from May to August as well as the overall ranking based on the mean RMSD of the model across all months.

Model	Group	Overall	May	June	July	August
EC-Earth3-CC	WB	1	4	4	2	1
EC-Earth3-Veg-LR	WB	2	1	1	7	5
EC-Earth3-AerChem	WB	3	2	6	6	2
CMCC-CM2-SR5	WB	4	6	2	3	9
TaiESM1	WB	5	9	5	1	3
CMCC-ESM2	WB	6	3	3	9	8
EC-Earth3	WB	7	5	8	10	4
CMCC-CM2-HR4	WB	8	10	9	4	7
NorESM2-LM	WB	9	12	10	8	10
NorESM2-MM	WB	10	14	15	5	6
MPI-ESM1-2-HR	WB	11	11	7	11	14
NESM3	WB	12	8	13	15	11
MPI-ESM1-2-LR	WB	13	19	12	12	13
INM-CM5-0	WB	14	18	14	13	12
CanESM5	WB	15	7	11	20	17
AWI-ESM-1-1-LR	WB	16	17	19	17	16
CNRM-ESM2-1	EB	17	16	18	18	20
CNRM-CM6-1	EB	18	21	17	19	19
BCC-ESM1	WB	19	13	16	29	26
MPI-ESM-1-2-HAM	WB	20	34	23	14	18
INM-CM4-8	WB	21	36	28	16	15
SAM0-UNICON	EB	22	23	20	22	22
FGOALS-f3-L	EB	23	33	21	21	21
GFDL-CM4	EB	24	15	35	26	24
CESM2	EB	25	32	26	25	23
CESM2-WACCM	EB	26	31	27	24	28
IPSL-CM6A-LR-INCA	EB	27	29	24	28	31
IPSL-CM6A-LR	EB	28	28	22	32	33
MIROC6	EB	29	24	25	35	30
HadGEM3-GC31-MM	EB	30	27	34	30	27
MRI-ESM2-0	EB	31	26	29	33	29
HadGEM3-GC31-LL	EB	32	20	30	34	36
UKESM1-0-LL	EB	33	30	32	31	35
FGOALS-g3	EB	34	37	31	23	25
ACCESS-ESM1-5	EB	35	35	33	27	32
KACE-1-0-G	EB	36	25	36	36	34
ACCESS-CM2	EB	37	22	37	37	37
IITM-ESM	WB	38	38	38	38	38

Note: Group indicates the sub-setting based on centre of action longitude anomalies in May (see main text for detailed description). The table has been reordered based on the overall rankings of MYF detection density.

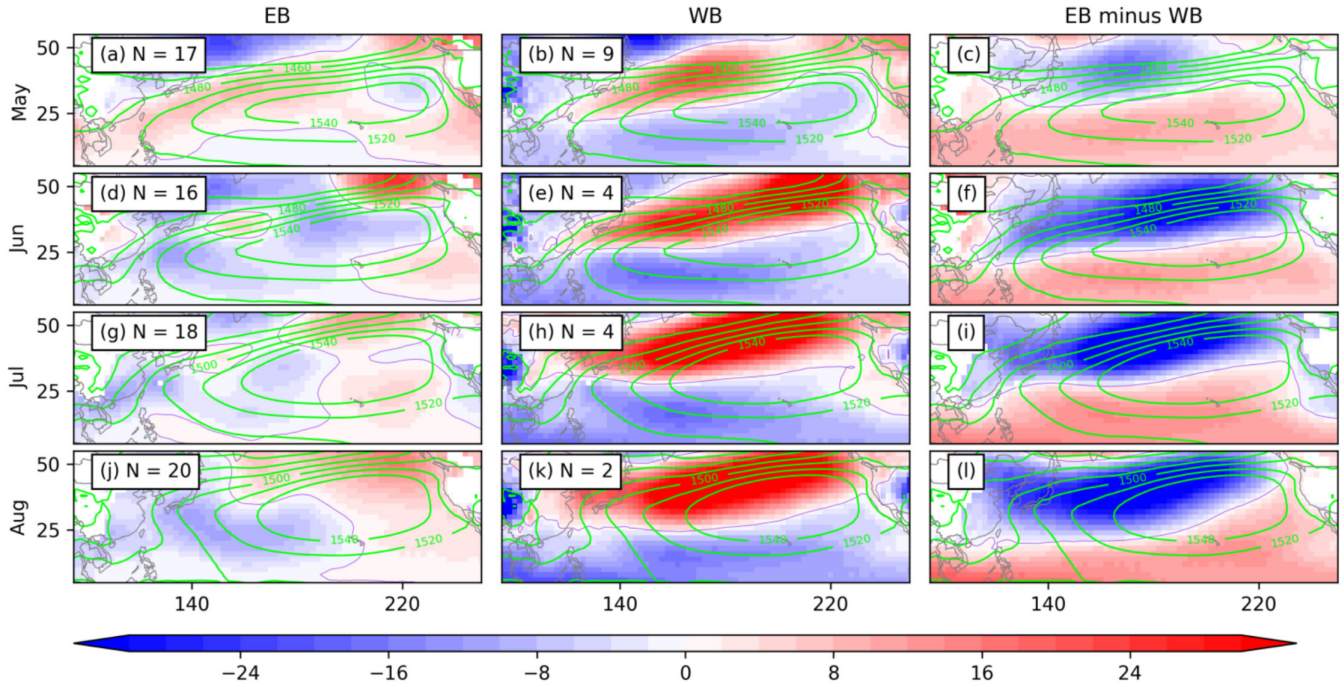

FIGURE 4 | Composites of 850 hPa geopotential height anomalies (in unit of gpm) of models with significant eastward bias (EB; left column) and significant westward bias (WB; middle column) in centre of action with respect to ERA5; and the composite of the difference in 850 hPa geopotential height between these two bias groups (right column). The green contours show the ERA5 850 hPa geopotential height climatology of the respective months. The number of models (*N*) used in composite is shown on the top left of the respective panels. [Colour figure can be viewed at wileyonlinelibrary.com]

and WB in the Western North Pacific (Figure 4). In other words, the WNPSH-N effectively captures the core differences between these two patterns.

In the case of EB, there are spatially extensive negative geopotential height anomalies over the western central North Pacific from June to August (Figure 4d,g,j). This leads to an anomalous east/northeasterly moisture flux and positive anomalous moisture divergence within the region of the climatological MYF detection density in ERA5 (Figure 5d,g,j), while the positive anomalous moisture convergence can be found in the south/southeast of the region of the climatological MYF detection density in ERA5. This promotes the establishment of the MYF in the south/southeast of the climatological position of the MYF detection density (Figure S2) while hindering its westward extension due to reduced moisture flux in the region.

In the case of WB, a basin-wide dipole pattern emerges with positive geopotential height anomalies in the north and northwest side of the North Pacific and negative geopotential height anomalies in the south and southwest side of the North Pacific (Figure 4b,e,h,k). The positive geopotential anomalies strengthen and expand southward as the season progresses. This leads to an increase in east/southeasterly anomalous moisture flux over the Western North Pacific (WNP), particularly over the East China Sea, and an increase in anomalous convergence over the continental east China while there is a decrease in convergence over the East China Sea and the Yellow Sea (Figure 5b,e,h,k). This phenomenon suppresses the eastward extension of the MYF due to a lack of eastward moisture flux and weaker moisture convergence over the ocean, resulting in the WB pattern.

To summarize, the evolution of the east–west MYF detection density bias in CMIP6 models can be understood as follows: For EB, as the EASM season progresses, the negative geopotential height anomalies over the western central North Pacific develop and persist while the western edge of the NPH shifts northward (Figure S3). This indicates that the NPH in CMIP6 models in the group EB is consistently weak, leading to weaker moisture flux and convergence into the observed MYF detection region, but stronger moisture convergence over the southeastern side of the observed MYF detection region. For WB, the dipole pattern in the geopotential height anomalies in the north of the central Pacific strengthens as the EASM season progresses. This leads to a reduction of the moisture flux and moisture convergence over the eastern side of the observed MYF detection region.

3.2.2 | Representations of North Pacific High for North–South Centre of Action Bias

Similar analyses, as in Section 3.2.1, have been conducted for the monthly climatological composite anomalies constructed using models with significant CoA northward bias (NB) and south bias (SB) (Figures 6 and 7). It should be noted that, for a given model, there is no clear link between east–west CoA bias and north–south CoA bias (Table S1).

Figure 6 shows the NB (Figure 6a,b,e,h) and SB (Figure 6c,f,i) composites of 850 hPa geopotential height anomalies, relative to the ERA5 monthly climatology. In the NB composites (Figure 6a,b,e,h), it can be seen that there are large-scale positive geopotential height anomalies over the north/northwestern side of NPH and relatively weak negative geopotential

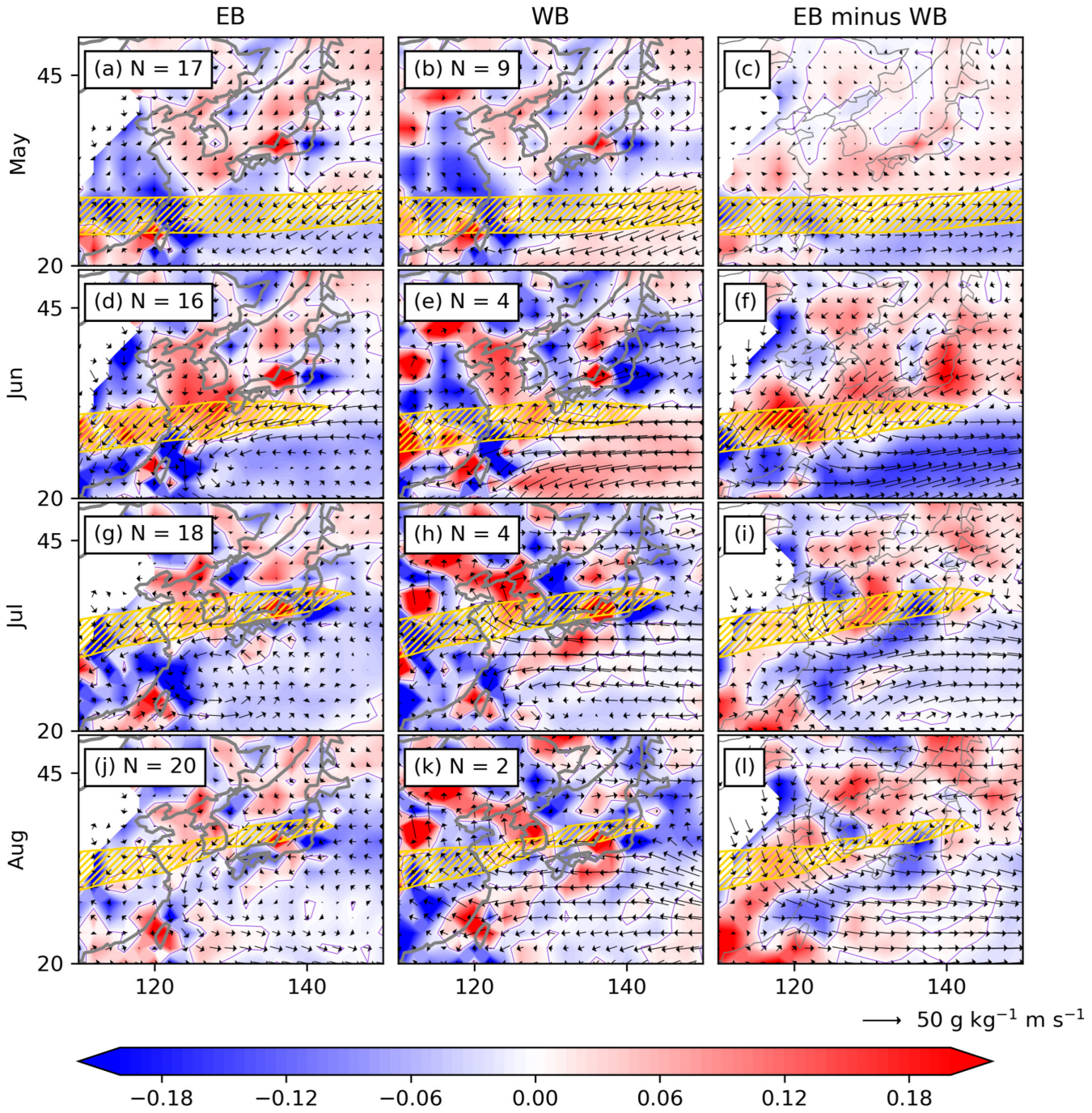

FIGURE 5 | Composites of 850 hPa moisture flux anomalies (quivers; in unit of g kg^{-1} m s^{-1}) and moisture flux divergence anomalies (colour contours; in unit of 10^{-4} g kg^{-1} s^{-1}; blue for abnormal convergence, thus frontogenetic, red for abnormal divergence, thus frontolytic) of models with significant eastward bias (left column) and significant westward bias (middle column) in centre of action with respect to ERA5; and the composite of the difference in 850 hPa moisture flux anomalies (quivers) and moisture flux divergence anomalies (colour contours) between these two bias groups (right column). The yellow contours with hatches show the region of climatological Mei-yu front detection density in ERA5 of the respective months that is above 0.5. The number of models (*N*) used in composite is shown on the top left of the respective panels. [Colour figure can be viewed at wileyonlinelibrary.com]

height anomalies over the tropical central north Pacific, but this does not extend to the East China Sea. The positive geopotential height anomalies strengthen and expand to the south in June, then retreat and weaken in July and August (Figure 6b,e,h). On the other hand, there are large-scale negative anomalies over the central and western north Pacific, which also extend to the East China Sea and East China, in the SB composites (Figure 6c,f,i). At the same time, positive anomalies to the north of the NPH grow larger and stronger as the season progresses. Comparing the 850 hPa geopotential height composites of NB and SB (Figure 6d,g,j) shows large positive anomalies extending to east China and the East China Sea while negative anomalies grow on the north/northwestern side of the NPH.

The north–south bias of the MYF detection density in CMIP6 models is also associated with the WNPSH. In May, there is a significant correlation between the north–south bias of the MYF detection density in CMIP6 and WNPSH-N ($r=0.569$, p-value$=0.0002$; Table 3). Given that the only north–south bias in May is in NB, the physical explanation can be understood as follows: In CMIP6 models, due to the large positive 850 hPa geopotential height anomalies in the north/northwest of the NPH and negative anomalies over the central and western North Pacific (Figure 6a), anomalous south-westerly (easterly) moisture flux over east (south) China, along with anomalous moisture convergence (divergence), promotes (suppresses) the formation of the MYF over East (South) China (Figure 7a). Consequently, this leads to a northward bias in the MYF detection density climatology in CMIP6 models. The positive 850 hPa geopotential height anomalies in the north/northwest of the NPH are well represented by WNPSH-N.

TABLE 3 | Pearson's correlation coefficient of the centre of action latitude (longitude) anomalies versus climatological Western North Pacific Subtropical High indices calculated using all models.

Month	Indices	CoA latitude anomalies	CoA longitude anomalies
May	WNPSH-W	0.174	0.083
	WNPSH-N	0.569*	−0.219
June	WNPSH-W	0.355*	−0.122
	WNPSH-N	0.494*	−0.456*
July	WNPSH-W	0.407*	−0.089
	WNPSH-N	0.259	−0.535*
August	WNPSH-W	0.231	−0.156
	WNPSH-N	−0.069	−0.498*

Note: Asterisks indicate correlations are significant at 0.05 levels.

In June, the north–south bias of the MYF detection density in CMIP6 models is significantly correlated with both WNPSH-N ($r=0.494$, p-value$=0.0016$) and WNPSH-W ($r=0.355$, p-value$=0.0289$). This correlation is linked to the extensive positive and negative geopotential height anomalies over the western edge of the NHP for the NB and SB cases, respectively (Figure 6b,c). For NB (Figure 7b), anomalous easterly moisture flux over the western North Pacific and the East China Sea suppresses the formation of the MYF at lower latitudes. In the case of SB (Figure 7c), anomalous northerly/easterly/north-easterly moisture flux over East China, the East China Sea, and the south of Japan, combined with weak moisture convergence, suppresses the MYF formation at observed climatological latitudes. Meanwhile, enhanced moisture convergence in the southern part of the Western North Pacific facilitates the MYF formation, leading to SB. Figure 7d highlights the major differences in the climatological 850 hPa moisture flux between NB and SB. There is significantly more (less) moisture flux and moisture convergence over the northern (southern) part of the MYF domain, contributing to the north–south bias.

In July, the north–south bias of the MYF detection density in CMIP6 is significantly correlated with WNPSH-W ($r=0.407$, p-value$=0.0111$), but not with WNPSH-N ($r=0.259$, p-value$=0.1157$). Positive geopotential height anomalies appear in the north/northwest of the NPH in both NB and SB composites (Figure 6e,f), within the calculation domain of WNPSH-N. Conversely, negative and positive geopotential height anomalies

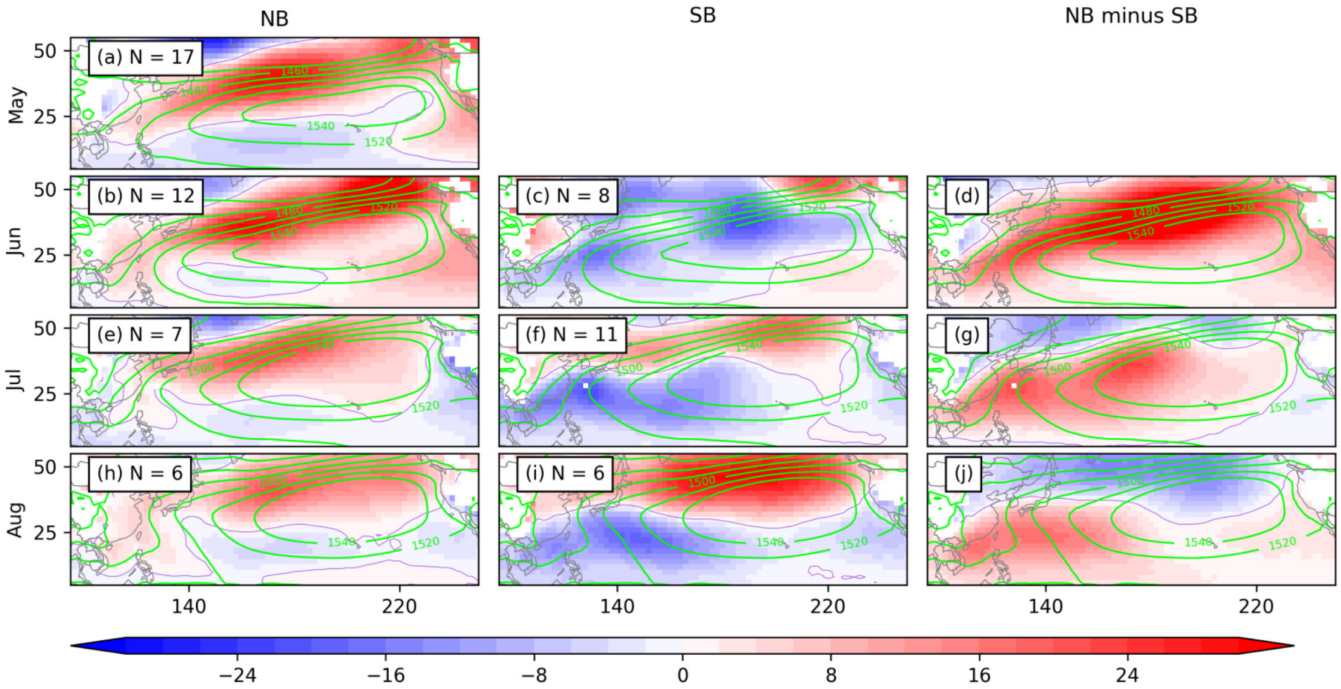

FIGURE 6 | As in Figure 4, but composites are constructed based on models with significant northward bias (NB) and significant southward bias (SB) in centre of action (CoA). Since no model has significantly southward bias in CoA in May, the May composite of significant southward bias and the difference between these two bias groups are not produced. [Colour figure can be viewed at wileyonlinelibrary.com]

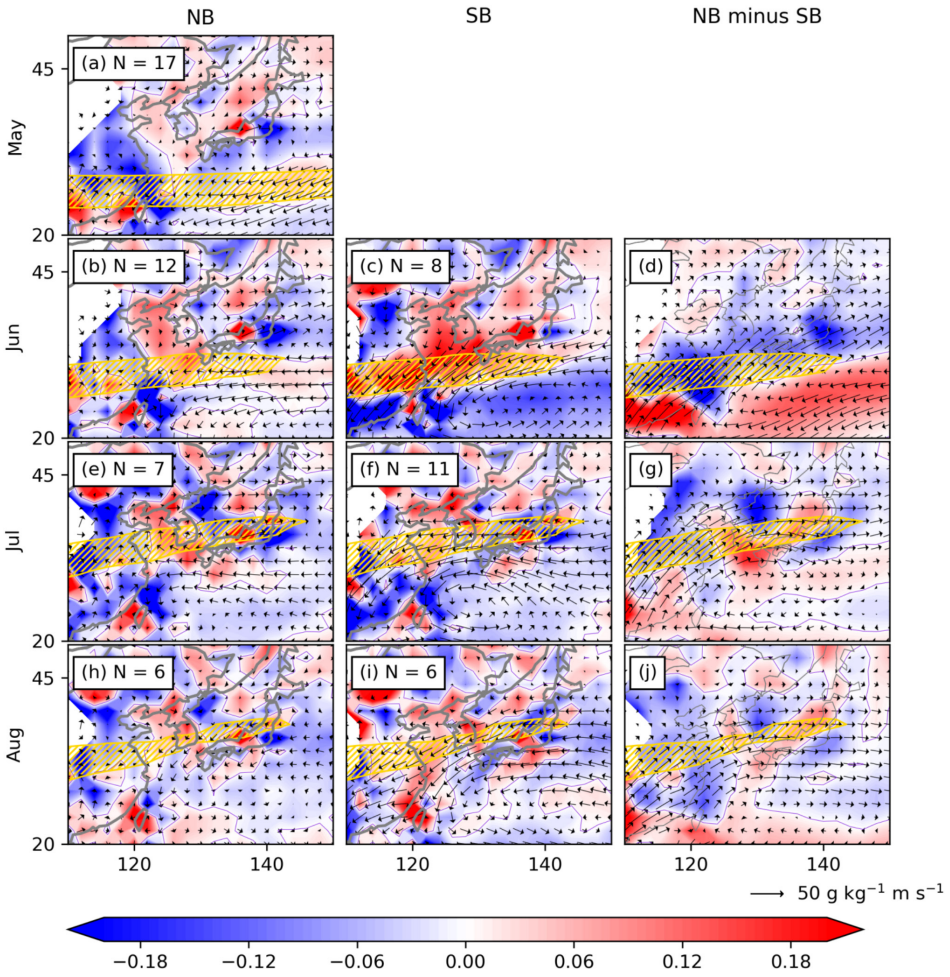

FIGURE 7 | As in Figure 5, but composites are constructed based on models with significant northward bias and significant southward bias. [Colour figure can be viewed at wileyonlinelibrary.com]

develop over the south/southwest of the NPH in SB and NB, respectively, which fall within the calculation domain of WNPSH-W. For NB, anomalous moisture convergence, coupled with anomalous southerly/southwesterly moisture flux over continental China, promotes MYF formation at higher latitudes, despite anomalous moisture divergence over the Yellow Sea (Figure 7e). In the case of SB (Figure 7f), anomalous easterly/northeasterly moisture flux, along with anomalous moisture divergence over East China, the Yellow Sea, and the East China Sea, suppresses MYF formation in the north. Figure 7g highlights the major differences in the climatological 850 hPa moisture flux between NB and SB. As in June, there is more (less) moisture flux and moisture convergence over the northern (southern) part of the MYF domain, contributing to the north–south bias. While similar observations can be made for the August composites (Figures 6 and 7), the north–south bias of MYF detection density in CMIP6 is not significantly correlated with WNPSH-W ($r = 0.231$, p-value $= 0.1635$) or WNPSH-N ($r = -0.069$, p-value $= 0.6796$). This indicates other factors are contributing to the biases.

To summarize, the evolution of the north–south MYF detection density bias in CMIP6 models can be understood as follows: For NB, the persistent large-scale positive geopotential height anomalies over the north/northwestern side of the NPH, which covers the East China Sea, lead to positive anomalous moisture convergence north of the observed MYF detection region; whereas for SB, the development of negative anomalies of geopotential height over the East China Sea is linked to negative moisture convergence anomalies in the observed MYF detection region and positive moisture convergence anomalies south of the observed MYF detection region.

4 | Discussion

4.1 | Potential Source of North Pacific High Bias in Climate Models

As shown in Section 3, the biases in the western edge of the NPH make significant contributions to the bias in the MYF detection density (Table 3). These biases may occur independently as well as simultaneously depending on the configuration of WNPSH as the monsoon season progresses. We have also shown that the eastward bias of the MYF detection density is linked to the representation of the NPH being weaker and smaller, particularly over the western Pacific region, in the models (Figure 4d,g,j). Consequently, models with weak and small NPH tend to have lower rankings, such as models from the HadGEM family. Rodríguez et al. (2017) and Rodríguez and Milton (2019) studied the EASM circulation bias in the climate simulations of a

variation of HadGEM2 (Williams et al. 2015) and a variation of HadGEM3 (Williams et al. 2018), respectively. Rodríguez et al. (2017) found that one of the systematic circulation errors in the HadGEM2 climate simulations is a weakening of the summer WNPSH, which leads to an underestimation of the southwesterly monsoon flow over the region, and a similar bias was found in HadGEM3 (Rodríguez and Milton 2019). Such bias ultimately affects the regional moisture transports and the representation of the monsoonal rainfall over China in the models. Through sensitivity experiments, Rodríguez and Milton (2019) identified the circulation error in the model that is associated with the excessive moisture divergence in the tropical boundary layer over the Maritime continent due to the deficiencies in tropical convection. They suggest that improvements in the convective parametrization scheme, such as the use of CoMorph (see appendix A of Daleu et al. 2023), could improve the representation of convective activity over the Maritime continent and consequently improve the representation of the WNPSH and the regional circulation and hence the representation of the MYF.

4.2 | Other Potential Sources of Bias

As shown in Table 3, the WNPSH indices can only explain roughly 30% of the variance in the CoA anomalies. This implies that other sources of bias are present, of which one important one will be discussed in the following, not meaning that there may not be other, further important bias sources. For example, the South Asian High (SAH; Ning et al. 2017) is another synoptic-scale atmospheric pattern, which is known to have a strong influence on the moisture supply to the EASM over East China. Ning et al. (2017) have shown that the strength (or the size) and orientation of SAH are closely related to extreme rainfall over east China during the EASM period. This, in essence, contributes to the moisture flux that is required for the formation of the MYF. Following Ning et al. (2017), the SAH is defined as the region of 200 hPa geopotential height above at least 12,500gpm within the South Asia domain.

Figure S7 shows the climatological SAH in ERA5 and the CMIP6 models. Comparing the SAH evolution in ERA5 (Figure S7xl) with the SAH evolution in the MME mean of the CMIP6 models (Figure S7xxxix), the SAH in the CMIP6 MME mean is only observed in July and August, whereas the SAH can be identified in ERA5 since June. Furthermore, the size, and consequently the strength, of the SAH in the CMIP6 MME mean is much smaller and weaker than the SAH in ERA5. On the other hand, the CMIP6 inter-model variability of SAH is large (Figure S7). Some models, such as CMCC-CM2-HR4, CMCC-CM2-SR5, CMCC-ESM2, CanESM5 and ACCESS-ESM1-5, have developed SAH in May, although the positions are largely displaced. While some models, such as IPSL-CM6A-LR, never develop a SAH for the entire summer, other models, such as CESM2 (Figure S7xxiii), generate exceptionally large and strong SAH in comparison to ERA5. This demonstrates that SAH could be another major source of bias.

4.3 | Transferability of Results for Performance Evaluations?

As outlined in the Introduction, several studies (Park et al. 2020; Bu et al. 2022) have examined the representation of different facets of climate models that are closely associated with the EASM. These aspects include the evolution of EASM precipitation (Park et al. 2020) and the regional circulation patterns in Asia (Bu et al. 2022). An intriguing question arises: can the performance of a model in one aspect of the EASM be used to infer its performance in other aspects of the same phenomenon? In this section, we undertake a comparative analysis of the performance rankings established in prior research and our current study.

The rankings from Park et al. (2020) have been rederived in our analysis, based on the pattern correlation coefficient between the Hovmöller diagram of observed precipitation and the Hovmöller diagram of CMIP6-simulated EASM precipitation (see tab. 4 of Park et al. 2020). Similarly, the rankings from Bu et al. (2022) have been rederived, which are considered a comprehensive metric that assesses the performance of each model (see tab. 2 of Bu et al. 2022), averaged across all variants of the same model. These rederived rankings are relative to a common set of models investigated across multiple studies and are compiled in Table S2.

Notably, our analysis reveals that models demonstrating good climatological representation in regional circulation patterns, such as CanESM5, do not necessarily exhibit corresponding excellence in climatological representation of EASM precipitation or the MYF. Conversely, models with robust climatological representation of MYF, like TaiESM1, may not excel in representing the regional circulation patterns or EASM precipitation. Furthermore, it is evident that these rankings exhibit low (but significant) to no correlations with each other (Table S3). This observation underscores that model rankings are not transferable and are specific to the particular aspects under investigation within each study. This demonstrates the complexity of the EASM.

5 | Summary and Conclusion

This study investigates the climatological representation of the MYF in 38 CMIP6 models in the period of May to August with respect to ERA5 using the MYF detection density and identifies the sources of bias. We found that many CMIP6 models cannot produce the MYF detection density climatology as observed in ERA5 and the performance of the models in simulating the MYF varies with the month of interest. The 38 CMIP6 models can be divided into two groups based on the east–west MYF detection density bias in May: models with bias less than 0° E (Group WB) or greater than 0° E (Group EB). These groups have distinct evolution pathways where models in Group WB, in general, have limited eastward bias in comparison to models in Group EB, and this observation holds for all months of interest. Based on the mean RMSD of MYF detection density over all months, we have identified models with the overall best and worst representation of MYF climatology.

We investigated the source of bias in the MYF detection density by looking into the representation of the NPH of the CMIP6 models using 850 hPa geopotential anomalies as well as the WNPSH indices (Lu 2002). We have shown that models with EB have spatially extensive negative anomalies over the west of

the central north Pacific, whereas models with WB have a basin-wide dipole pattern with positive anomalies in the north and/or northwest side of the north Pacific and negative anomalies in the south and/or southwest side of the north Pacific.

Through cross-model correlation analysis between WNPSH indices and CoA longitude anomalies, we quantitatively show that the June–August east–west bias in the MYF detection density is significantly linked to the northward extension of the western edge of the NPH. Similar analyses have been performed to understand the north–south bias of the MYF detection density where the WNPSH indices have been shown to be useful in capturing the essential anomalous patterns in the 850 hPa geopotential height anomalies. This is related to the anomalous 850 hPa moisture flux transport promoting and limiting the east–west extension of the MYF. Other potential sources of bias based on misrepresentation of the large-scale circulation have been discussed.

Furthermore, we have demonstrated that a successful model evaluation of certain aspects of the EASM does not necessarily translate well into other aspects of the EASM. This is due to the complexity of the EASM circulation. Further investigation is necessary to identify the source of biases in different aspects of EASM circulation from different models, which would consequently improve individual model ability in representing extreme events in the EASM.

Author Contributions

Kelvin S. Ng: conceptualization, investigation, writing – original draft, writing – review and editing, visualization, software, formal analysis, methodology. **Gregor C. Leckebusch:** conceptualization, methodology, writing – original draft, supervision, writing – review and editing, funding acquisition. **Kevin I. Hodges:** conceptualization, writing – original draft, writing – review and editing, funding acquisition, methodology, supervision. **Yaocun Zhang:** conceptualization, writing – review and editing.

Acknowledgements

This work was supported by the UK-China Research and Innovation Partnership Fund through the Met Office Climate Science for Service Partnership (CSSP) China as part of the Newton Fund. The calculations described in this paper were performed using the BlueBEAR HPC service at the University of Birmingham and JASMIN, the collaborative data analysis facility.

Conflicts of Interest

The authors declare no conflicts of interest.

Data Availability Statement

The data that support the findings of this study are available from the corresponding author upon reasonable request.

References

Andrews, M. B., J. K. Ridley, R. A. Wood, et al. 2020. "Historical Simulations With HadGEM3-GC3.1 for CMIP6." *Journal of Advances in Modeling Earth Systems* 12: e2019MS001995.

Befort, D. J., K. Hodges, and G. C. Leckebusch. 2016. "East Asian Rainfall in CMIP5 Models: Contribution of Tropical Cyclones and Mei-Yu Front to Spatio-Temporal Rainfall Variability." *AGU Fall Meeting* 2016: A23J–A0365J.

Befort, D. J., K. Hodges, and G. C. Leckebusch. 2017. "A New Approach for Estimating Projected Future Changes in Extreme Rainfall Over East Asia and Its Uncertainties Including Information About Model Performance on Different Scales." *AGU Fall Meeting* 2017: A53C–A1476C.

Befort, D. J., T. Kruschke, and G. C. Leckebusch. 2020. "Objective Identification of Potentially Damaging Tropical Cyclones Over the Western North Pacific." *Environmental Research Communications* 2: 031005.

Bi, D., M. Dix, S. Marsland, et al. 2020. "Configuration and Spin-Up of ACCESS-CM2, the New Generation Australian Community Climate and Earth System Simulator Coupled Model." *Journal of Southern Hemisphere Earth Systems Science* 70: 225–251.

Boucher, O., J. Servonnat, A. L. Albright, et al. 2020. "Presentation and Evaluation of the IPSL-CM6A-LR Climate Model." *Journal of Advances in Modeling Earth Systems* 12: e2019MS002010.

Bu, L., Z. Zuo, and N. An. 2022. "Evaluating Boreal Summer Circulation Patterns of CMIP6 Climate Models Over the Asian Region." *Climate Dynamics* 58: 427–441.

Cao, J., B. Wang, Y. M. Yang, et al. 2018. "The NUIST Earth System Model (NESM) Version 3: Description and Preliminary Evaluation." *Geoscientific Model Development* 11: 2975–2993.

Cherchi, A., P. G. Fogli, T. Lovato, et al. 2019. "Global Mean Climate and Main Patterns of Variability in the CMCC-CM2 Coupled Model." *Journal of Advances in Modeling Earth Systems* 11: 185–209.

Daleu, C. L., R. S. Plant, A. J. Stirling, and M. Whitall. 2023. "Evaluating the CoMorph-A Parametrization Using Idealized Simulations of the Two-Way Coupling Between Convection and Large-Scale Dynamics." *Quarterly Journal of the Royal Meteorological Society* 149: 3087–3109.

Danabasoglu, G., J. F. Lamarque, J. Bacmeister, et al. 2020. "The Community Earth System Model Version 2 (CESM2)." *Journal of Advances in Modeling Earth Systems* 12: e2019MS001916.

Ding, Y., and J. C. L. Chan. 2005. "The East Asian Summer Monsoon: An Overview." *Meteorology and Atmospheric Physics* 89: 117–142.

Ding, Y., P. Liang, Y. Liu, and Y. Zhang. 2020. "Multiscale Variability of Meiyu and Its Prediction: A New Review." *Journal of Geophysical Research: Atmospheres* 125: e2019JD031496.

Ding, Y., Y. Liu, and Z.-Z. Hu. 2021. "The Record-Breaking Meiyu in 2020 and Associated Atmospheric Circulation and Tropical SST Anomalies." *Advances in Atmospheric Sciences* 38: 1980–1993.

Döscher, R., M. Acosta, A. Alessandri, et al. 2022. "The EC-Earth3 Earth System Model for the Coupled Model Intercomparison Project 6." *Geoscientific Model Development* 15: 2973–3020.

Eyring, V., S. Bony, G. A. Meehl, et al. 2016. "Overview of the Coupled Model Intercomparison Project Phase 6 (CMIP6) Experimental Design and Organization." *Geoscientific Model Development* 9: 1937–1958.

Gutjahr, O., D. Putrasahan, K. Lohmann, et al. 2019. "Max Planck Institute Earth System Model (MPI-ESM1.2) for the High-Resolution Model Intercomparison Project (HighResMIP)." *Geoscientific Model Development* 12: 3241–3281.

He, B., Y. Yu, Q. Bao, et al. 2020. "CAS FGOALS-f3-L Model Dataset Descriptions for CMIP6 DECK Experiments." *Atmospheric and Oceanic Science Letters* 13: 582–588.

Held, I. M., H. Guo, A. Adcroft, et al. 2019. "Structure and Performance of GFDL's CM4.0 Climate Model." *Journal of Advances in Modeling Earth Systems* 11: 3691–3727.

Hersbach, H., B. Bell, P. Berrisford, et al. 2020. "The ERA5 Global Reanalysis." *Quarterly Journal of the Royal Meteorological Society* 146: 1999–2049.

Horinouchi, T., Y. Kawatani, and N. Sato. 2023. "Inter-Model Variability of the CMIP5 Future Projection of Baiu, Meiyu, and Changma Precipitation." *Climate Dynamics* 60: 1849–1864.

Kuma, P., F. A. M. Bender, and A. R. Jönsson. 2023. "Climate Model Code Genealogy and Its Relation to Climate Feedbacks and Sensitivity." *Journal of Advances in Modeling Earth Systems* 15: e2022MS003588.

Lee, J., J. Kim, M.-A. Sun, et al. 2020a. "Evaluation of the Korea Meteorological Administration Advanced Community Earth-System Model (K-ACE)." *Asia-Pacific Journal of Atmospheric Sciences* 56: 381–395.

Lee, W. L., Y. C. Wang, C. J. Shiu, et al. 2020b. "Taiwan Earth System Model Version 1: Description and Evaluation of Mean State." *Geoscientific Model Development* 13: 3887–3904.

Li, L., Y. Yu, Y. Tang, et al. 2020. "The Flexible Global Ocean-Atmosphere-Land System Model Grid-Point Version 3 (FGOALS-g3): Description and Evaluation." *Journal of Advances in Modeling Earth Systems* 12: e2019MS002012.

Lu, R. Y. 2002. "Indices of the Summertime Western North Pacific Subtropical High." *Advances in Atmospheric Sciences* 19: 1004–1028.

Massonnet, F., M. Ménégoz, M. Acosta, X. Yepes-Arbós, E. Exarchou, and F. J. Doblas-Reyes. 2020. "Replicability of the EC-Earth3 Earth System Model Under a Change in Computing Environment." *Geoscientific Model Development* 13: 1165–1178.

Neubauer, D., S. Ferrachat, C. Siegenthaler-Le Drian, et al. 2019. "The Global Aerosol–Climate Model ECHAM6.3–HAM2.3 – Part 2: Cloud Evaluation, Aerosol Radiative Forcing, and Climate Sensitivity." *Geoscientific Model Development* 12: 3609–3639.

Ng, K. S., and G. C. Leckebusch. 2021. "A New View on the Risk of Typhoon Occurrence in the Western North Pacific." *Natural Hazards and Earth System Sciences* 21: 663–682.

Ng, K. S., G. C. Leckebusch, and K. I. Hodges. 2022. "A Causality-Guided Statistical Approach for Modeling Extreme Mei-Yu Rainfall Based on Known Large-Scale Modes – A Pilot Study." *Advances in Atmospheric Sciences* 39: 1925–1940.

Ng, K. S., G. C. Leckebusch, and K. I. Hodges. 2024. "Improvement of Decadal Predictions of Monthly Extreme Mei-Yu Rainfall via a Causality Guided Approach." *Environmental Research: Climate* 3: 041001.

Ning, L., J. Liu, and B. Wang. 2017. "How Does the South Asian High Influence Extreme Precipitation Over Eastern China?" *Journal of Geophysical Research: Atmospheres* 122: 4281–4298.

Osinski, R., P. Lorenz, T. Kruschke, et al. 2016. "An Approach to Build an Event Set of European Windstorms Based on ECMWF EPS." *Natural Hazards and Earth System Sciences* 16: 255–268.

Park, J., H. Kim, S. Y. Simon Wang, et al. 2020. "Intensification of the East Asian Summer Monsoon Lifecycle Based on Observation and CMIP6." *Environmental Research Letters* 15: 0940b9.

Park, S., J. Shin, S. Kim, E. Oh, and Y. Kim. 2019. "Global Climate Simulated by the Seoul National University Atmosphere Model Version 0 With a Unified Convection Scheme (SAM0-UNICON)." *Journal of Climate* 32: 2917–2949.

Piao, J., W. Chen, S. Chen, H. Gong, Z. Wang, and X. Lan. 2023. "How Well Do CMIP6 Models Simulate the Climatological Northern Boundary of the East Asian Summer Monsoon?" *Global and Planetary Change* 221: 104034.

Rackow, T., H. F. Goessling, T. Jung, et al. 2018. "Towards Multi-Resolution Global Climate Modeling With ECHAM6-FESOM. Part II: Climate Variability." *Climate Dynamics* 50: 2369–2394.

Rodríguez, J. M., and S. F. Milton. 2019. "East Asian Summer Atmospheric Moisture Transport and Its Response to Interannual Variability of the West Pacific Subtropical High: An Evaluation of the Met Office Unified Model." *Atmosphere* 10: 457.

Rodríguez, J. M., S. F. Milton, and C. Marzin. 2017. "The East Asian Atmospheric Water Cycle and Monsoon Circulation in the Met Office Unified Model." *Journal of Geophysical Research: Atmospheres* 122, no. 10: 10,246–10,265.

Séférian, R., P. Nabat, M. Michou, et al. 2019. "Evaluation of CNRM Earth System Model, CNRM-ESM2-1: Role of Earth System Processes in Present-Day and Future Climate." *Journal of Advances in Modeling Earth Systems* 11: 4182–4227.

Seland, Ø., M. Bentsen, D. Olivié, et al. 2020. "Overview of the Norwegian Earth System Model (NorESM2) and Key Climate Response of CMIP6 DECK, Historical, and Scenario Simulations." *Geoscientific Model Development* 13: 6165–6200.

Sellar, A. A., C. G. Jones, J. P. Mulcahy, et al. 2019. "UKESM1: Description and Evaluation of the U.K. Earth System Model." *Journal of Advances in Modeling Earth Systems* 11: 4513–4558.

Sidorenko, D., T. Rackow, T. Jung, et al. 2015. "Towards Multi-Resolution Global Climate Modeling With ECHAM6–FESOM. Part I: Model Formulation and Mean Climate." *Climate Dynamics* 44: 757–780.

Swapna, P., R. Krishnan, N. Sandeep, et al. 2018. "Long-Term Climate Simulations Using the IITM Earth System Model (IITM-ESMv2) With Focus on the South Asian Monsoon." *Journal of Advances in Modeling Earth Systems* 10: 1127–1149.

Swart, N. C., J. N. S. Cole, V. V. Kharin, et al. 2019. "The Canadian Earth System Model Version 5 (CanESM5.0.3)." *Geoscientific Model Development* 12: 4823–4873.

Tatebe, H., T. Ogura, T. Nitta, et al. 2019. "Description and Basic Evaluation of Simulated Mean State, Internal Variability, and Climate Sensitivity in MIROC6." *Geoscientific Model Development* 12: 2727–2765.

Tegen, I., D. Neubauer, S. Ferrachat, et al. 2019. "The Global Aerosol–Climate Model ECHAM6.3–HAM2.3 – Part 1: Aerosol Evaluation." *Geoscientific Model Development* 12: 1643–1677.

Thompson, V., N. J. Dunstone, A. A. Scaife, et al. 2017. "High Risk of Unprecedented UK Rainfall in the Current Climate." *Nature Communications* 8: 107.

Tomita, T., T. Yamaura, and T. Hashimoto. 2011. "Interannual Variability of the Baiu Season Near Japan Evaluated From the Equivalent Potential Temperature." *Journal of the Meteorological Society of Japan. Series II* 89: 517–537.

United Nations, Department of Economic and Social Affairs, Population Division. 2022. *World Population Prospects 2022*. United Nations, Department of Economic and Social Affairs, Population Division.

Voldoire, A., D. Saint-Martin, S. Sénési, et al. 2019. "Evaluation of CMIP6 DECK Experiments With CNRM-CM6-1." *Journal of Advances in Modeling Earth Systems* 11: 2177–2213.

Volodin, E. M., E. V. Mortikov, S. V. Kostrykin, et al. 2017. "Simulation of the Present-Day Climate With the Climate Model INMCM5." *Climate Dynamics* 49: 3715–3734.

Volodin, E. M., E. V. Mortikov, S. V. Kostrykin, et al. 2018. "Simulation of the Modern Climate Using the INM-CM48 Climate Model." *Russian Journal of Numerical Analysis and Mathematical Modelling* 33: 367–374.

Wainwright, C. M., E. Black, and R. P. Allan. 2021. "Future Changes in Wet and Dry Season Characteristics in CMIP5 and CMIP6 Simulations." *Journal of Hydrometeorology* 22: 2339–2357.

Wei, K., C. Ouyang, H. Duan, et al. 2020. "Reflections on the Catastrophic 2020 Yangtze River Basin Flooding in Southern China." *Innovation* 1: 100038.

Williams, K. D., D. Copsey, E. W. Blockley, et al. 2018. "The Met Office Global Coupled Model 3.0 and 3.1 (GC3.0 and GC3.1) Configurations." *Journal of Advances in Modeling Earth Systems* 10: 357–380.

Williams, K. D., C. M. Harris, A. Bodas-Salcedo, et al. 2015. "The Met Office Global Coupled Model 2.0 (GC2) Configuration." *Geoscientific Model Development* 8: 1509–1524.

Wu, P., R. Clark, K. Furtado, C. Xiao, Q. Wang, and R. Sun. 2023. "A Case Study of the July 2021 Henan Extreme Rainfall Event: From Weather Forecast to Climate Risks." *Weather and Climate Extremes* 40: 100571.

Wu, T., F. Zhang, J. Zhang, et al. 2020. "Beijing Climate Center Earth System Model Version 1 (BCC-ESM1): Model Description and Evaluation of Aerosol Simulations." *Geoscientific Model Development* 13: 977–1005.

Yang, K., W. Cai, G. Huang, K. Hu, B. Ng, and G. Wang. 2022. "Increased Variability of the Western Pacific Subtropical High Under Greenhouse Warming." *Proceedings of the National Academy of Sciences of the United States of America* 119: e2120335119.

Yukimoto, S., H. Kawai, T. Koshiro, et al. 2019. "The Meteorological Research Institute Earth System Model Version 2.0, MRI-ESM2.0: Description and Basic Evaluation of the Physical Component." *Journal of the Meteorological Society of Japan. Series II* 97: 931–965.

Zhou, T., L. Ren, and W. Zhang. 2021. "Anthropogenic Influence on Extreme Meiyu Rainfall in 2020 and Its Future Risk." *Science China Earth Sciences* 64: 1633–1644.

Ziehn, T., M. A. Chamberlain, R. M. Law, et al. 2020. "The Australian Earth System Model: ACCESS-ESM1.5." *Journal of Southern Hemisphere Earth Systems Science* 70: 193–214.

Supporting Information

Additional supporting information can be found online in the Supporting Information section.

Appendix A

Table of Acronym

Acronym	Full name
CMIP	Coupled Model Intercomparison Project
CoA	The monthly MYF detection density climatological mean centre of action
EASM	East Asian Summer Monsoon
EB	Eastward bias
ECMWF	European Centre for Medium-Range Weather Forecasts
ERA5	The fifth generation ECMWF reanalysis data
MME	Multi-model ensemble
MYF	Mei-yu front
NB	Northward bias
NPH	North Pacific High
r	Pearson's correlation coefficient
RMSD	Root mean squared differences
SAH	South Asian High
SB	Southward bias
WB	Westward bias
WNPSH	Western North Pacific Subtropical High
WNPSH-N	Lu's (2002) north index of WNPSH
WNPSH-W	Lu's (2002) west index of WNPSH